Thermally created Single-Photon Emitters in WS_2 monolayer

Gyeongjun Lee[1], Antoine Borel[1], Fausto Sirotti[1], and Fabian Cadiz[1]

[1]Laboratoire de Physique de la Matière Condensée, École Polytechnique, IP Paris, France

*Email: gyeongjun.lee@polytechnique.edu

Abstract

Single-photon emitters (SPEs) in solid-state materials enable scalable quantum communication and information processing. In two-dimensional semiconductors, however, controlled generation of optically active point defects remains challenging. Here, we use *in situ* high-temperature annealing of hBN-encapsulated monolayer WS$_2$ on a suspended micro-heater to produce a localized exciton emitter. Annealing around 1100 K leads to the emergence of an utlra-sharp emission line, X_L, located around 80 meV below the neutral exciton. X_L displays a resolution-limited linewidth at 0.2 meV, a radiative lifetime of ∼0.9 ns. Photoluminescence excitation spectroscopy shows that X_L originates from intrinsic excitons trapped at vacancy-like defects generated during annealing. Photon correlation measurments $g^2(\tau)$ shows clear antibunching with $g^{(2)}(0) \approx 0.4$, proving single quantum emitter. This approach provides a controlled and robust pathway for engineering SPEs in monolayer WS$_2$ and highlights the potential of defect-based quantum light sources in 2D semiconductors.
My name is gyeongjun

Introduction

Since the discovery of graphene [1], research on atomically thin materials has accelerated, particularly for transition metal dichalcogenides (TMDs) such as MoS$_2$, WS$_2$, and WSe$_2$ thanks to the isolation of atomically thin semiconductors based on TMDs, such as MoS$_2$ and WSe$_2$ [2, 3].

Their electronic structure also changes markedly with thickness. Bulk TMDs have an indirect bandgap, whereas monolayers exhibit a direct bandgap associated with the two inequivalent and spin-polarized valleys located at the K and K′ points of the Brillouin zone [2, 3].

The reduced dielectric screening and strong quantum confinement in monolayer TMDs enhance the Coulomb interaction [4], so that excitons dominate their optical properties at low temperature [5]. Monolayer TMDs host tightly bound excitons with large oscillator strength, making them suitable for quantum photonics and integrated optoelectronics. Their small Bohr radius and weak dielectric screening make excitons highly sensitive to local perturbations, so that defects, strain, or dielectric disorder can easily confine excitons [6]. Single-photon emission from such defect-bound excitons has been observed in monolayer TMDs, including WSe$_2$ [7] and vacancy-engineered MoS$_2$, where sulfur vacancies created by electron or ion irradiation, as well as by thermal annealing, act as deep confinement centers [8].

In this work, we use controlled thermal annealing as a means to generate defects in monolayer WS$_2$. We fabricate hBN/WS$_2$/hBN heterostructures on the suspended SiC membrane of a commercial micro-heater chip. The micro-heater is then integrated in a cryostat, allowing local Joule heating of the membrane up to ∼1200 K while the surrounding environment is kept at a few kelvin. We demonstrate that controlled thermal annealing enables the formation of single quantum emitters in monolayer WS$_2$. The resulting single-photon emission arises from excitons localized at defect sites generated during the annealing process.

Results and discussion

hBN-encapsulated WS$_2$ on micro-heater membranes

Fully encapsulated WS$_2$ monolayers were prepared by mechanical exfoliation of bulk crystals and assembly of hBN/WS$_2$/hBN heterostructures on Si/SiO$_2$ substrates. The stack was then picked up using a PC stamp and transferred onto the suspended SiC membrane of a Protochips micro-heater as shown in Figure 1(a) with thermal release at $\sim 200°$C. Figure 1(b) shows the hBN encapsulated monolayer WS_2 on SiC membrane.

Figure 1(c) represents the low temperature PL spectrum of the encapsulated WS$_2$, showing sharp excitonic resonances, including the neutral exciton X^0, negatively charged trions, dark-exciton related features, and phonon replicas with linewidths of only a few meV [9]. The observation of complex excitonic species and biexcitons confirms the excellent optical quality of the samples and the effectiveness of encapsulation in suppressing dielectric disorder.

Photoluminescence excitation (PLE) spectroscopy, in which the detection energy is fixed while the excitation energy is scanned, probes the absorption pathways that populate a given emission line. An increase in PL intensity indicates that the excitation is resonant with an excitonic transition, allowing PLE to map the absorption spectrum linked to that state. Our PLE data in Figure 1(d) reveals clear resonances at the A and B excitons and at the 2s excited states of the A exciton and the trion. The agreement between PL and PLE spectra shows that the excitonic structure is preserved after transfer and provides a reference for identifying new features that arise after annealing.
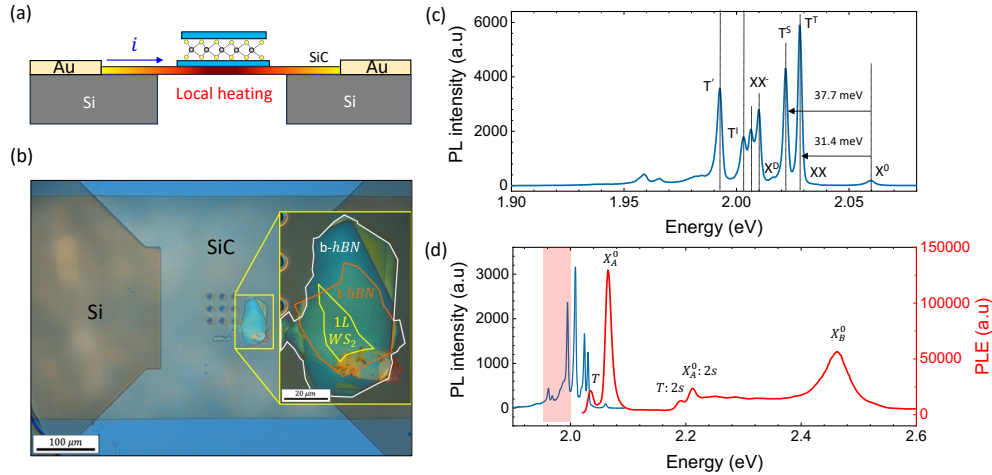

Figure 1: **Optical characterization of hBN-encapsulated monolayer WS$_2$ on a micro-heater membrane.** (a) Schematic of the micro-heater chip showing the suspended SiC membrane between metallic contacts and the hBN/WS$_2$/hBN stack transferred on top. (b) Optical image of a representative encapsulated flake on the membrane. (c) Low-temperature PL spectrum at 3.6K displaying sharp neutral-exciton, trion, and dark-state related resonances with linewidths of a few meV. ($\lambda_{\text{laser}} = 514.5$ nm, $P_{\text{laser}} = 1$ μW) (d) PLE spectrum highlighting well-resolved A- and B-exciton absorption resonances and higher-lying excitonic states. Graphics are placeholders; experimental data will be inserted once figures are prepared.($P_{\text{laser}} = 4$ μW)

Thermal annealing and emergence of the localized exciton X_{L}

Thermal annealing was performed *in situ* by driving a dc current through the suspended SiC membrane inside a closed-cycle cryostat. For each annealing step the current was increased to reach a target temperature, held for typically 30 min, and then turned off, after which the membrane cooled back to the base temperature of a few kelvin. For the temperature calibration, we measured PL spectrum at each annealing temperature as shown in Figure 2(a) and compared position of the neutral exciton peak using Pässler's model for the bandgap renormalization [10], which allowed us to extend the calibration up to $\sim$900 K by extrapolating to higher temperatures.

Up to ~1000 K the PL spectra remain dominated by the intrinsic excitonic features, apart from small reversible energy shifts and intensity changes. After annealing around 1100 K, an ultra sharp emission appears on the low-energy side of X^0. Figure 2(b,c) show the emergence of narrow emissions. The emission line X_L located about 80 meV below the neutral exciton.

In contrast to the few meV linewidths of the other excitonic peaks observed in as-exfoliated sample, X_L in encapsulated samples exhibits a linewidth below 0.2 meV at low excitation power, limited by the spectrometer resolution.
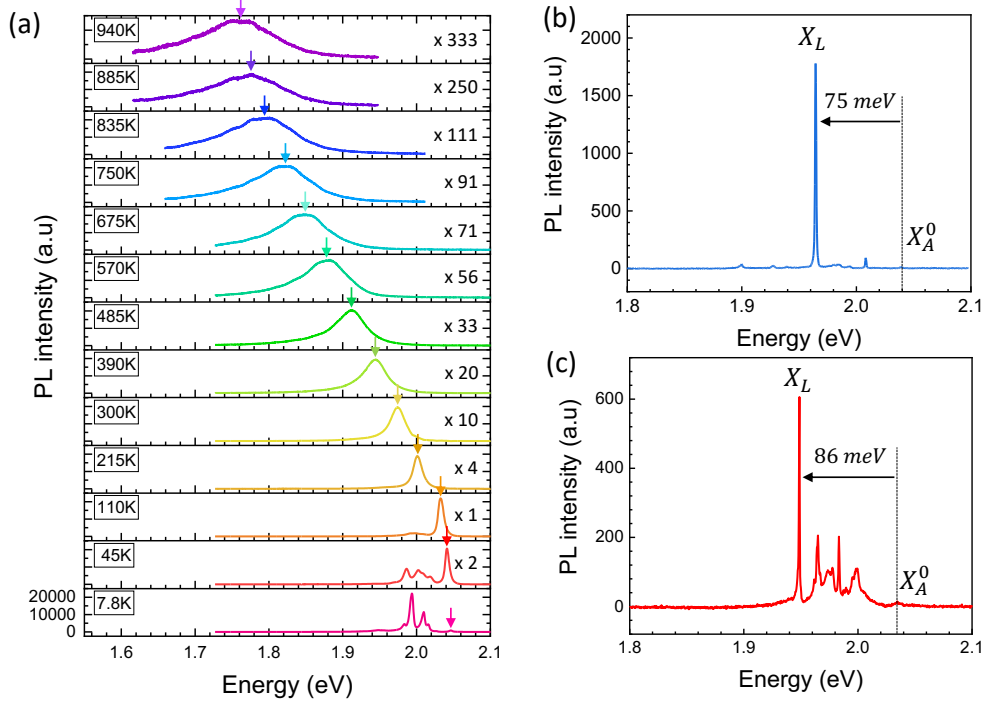

Figure 2: **Thermal-annealing-induced localized exciton emission in encapsulated WS$_2$.** (a) Low-temperature PL spectra at different annealing temperature, showing the red-shift of neutral exciton energy (X_A^0) (b) PL spectrum after annealing around 1100 K in the first sample $(\lambda_{\text{laser}}(CW) = 514.5$ nm, $P_{\text{laser}} = 1$ μW, $T = 3.65$ K). (c) PL spectrum after annealing around 1100 K in the second sample $(\lambda_{\text{laser}}(pulsed) = 503$ nm, $P_{\text{laser}} = 1$ μW, $T = 3.72$ K).

Excitonic origin and radiative dynamics of X_L

To identify the excitation pathway of X_L, we perform PLE spectroscopy only for the emission at the X_L energy while scanning the laser energy across the excitonic resonances. The PLE spectrum in Figure **??**(a) closely follows the absorption profile of the monolayer WS_2: it shows pronounced peaks at the A and B exciton energies and higher-lying states, mirroring the PLE recorded by as-exfoliated WS_2 (Figure 1(d)). This one-to-one correspondence demonstrates that X_L is populated by excitons created in the WS$_2$ bands rather than by extrinsic states in the substrate or encapsulation layers.

In addition, power-dependent PL measurements in Figure 3(b) confirm the defect nature of X_L. The integrated intensity initially increases linearly with excitation power and then saturates, as expected for a small number of defect sites that can host at most one exciton at a time. The linewidth of X_L broadens only weakly with power, which indicates that charge noise and local heating remain limited in the encapsulated structure.

Figure 3(c) shows time-resolved PL (TRPL) measurements. It indicates that the X_L emission decays with a characteristic lifetime of ~0.9 ns. This lifetime is significantly longer than that of trion emission in

the same sample, consistent with strong spatial localization suppressing nonradiative channels. The absence of a fast nonradiative component in the decay indicates that the defect potential defines a long-lived and efficient radiative recombination pathway.

The quantum nature of X_{L} is probed through second-order photon correlation measurements using a Hanbury Brown–Twiss setup under pulsed excitation. The measured intensity correlation function $g^{(2)}(\tau)$ shows a clear antibunching dip at zero delay with $g^{(2)}(0) \approx 0.3$ Figure 3(d), which unambiguously proves that X_{L} acts as a single-photon emitter. The moderate residual value of $g^{(2)}(0)$ is attributed to background emission and imperfect spectral filtering and can be further reduced by improving the collection optics and spectral selection.
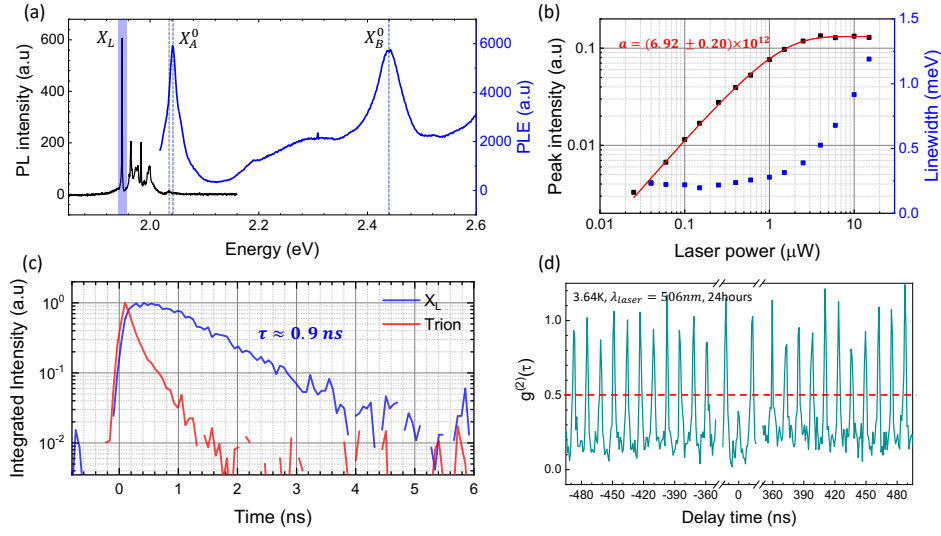

Figure 3: **Optical signatures of the localized exciton X_{L}.** (a) PLE spectrum recorded at the X_{L} emission energy, showing resonances at the A and B exciton absorption energies and higher-lying states. (b) Power dependence of the X_{L} intensity and linewidth, exhibiting saturation of the intensity and resolution-limited linewidth at low power. (c) Time-resolved PL traces of X_{L} and trion emission, highlighting the longer lifetime of the localized state. (d) Second-order correlation function $g^{(2)}(\tau)$ under pulsed excitation, displaying pronounced antibunching with $g^{(2)}(0) < 0.5$. Graphics are placeholders; experimental curves will be added in the final version.

Conclusion

We have demonstrated a controllable pathway to create single-photon emitters in hBN-encapsulated mono-layer WS$_2$ by *in situ* high-temperature annealing on a micro-heater platform. The clean dielectric environment provided by hBN enables the emergence of an ultra-narrow localized exciton X_{L} located around 80 meV below the neutral exciton after annealing around 1100 K. X_{L} exhibits a resolution-limited linewidth below 0.2 meV, a radiative lifetime of ∼0.9 ns, and clear photon antibunching with $g^{(2)}(0) \approx 0.3$, confirming its single-photon character. PLE and TRPL measurements show that X_{L} originates from intrinsic excitons captured by thermally generated vacancy-like defects that form deep, highly localized potentials.

Acknowledgements

Supporting information

Additional experimental details, micro-heater calibration procedures, extended temperature-dependent PL maps, PLE datasets, TRPL analysis, and raw $g^{(2)}(\tau)$ histograms will be provided in the Supporting Information.

The following files are available free of charge.

- SI_WS2_annealing.pdf: Experimental methods and additional figures.

- data_WS2_XL.zip: Selected raw PL, PLE, TRPL, and HBT data.

References

(1) Novoselov, K. S.; Geim, A. K.; Morozov, S. V.; Jiang, D.; Zhang, Y.; Dubonos, S. V.; Grigorieva, I. V.; Firsov, A. A. *Science* **2004**, *306*, 666–669.

(2) Radisavljevic, B.; Radenovic, A.; Brivio, J.; Giacometti, V.; Kis, A. *Nature Nanotechnology* **2011**, *6*, 147–150.

(3) Mak, K. F.; Lee, C.; Hone, J.; Shan, J.; Heinz, T. F. *Physical Review Letters* **2010**, *105*, 136805.

(4) Velický, M.; Toth, P. S. *Applied Materials Today* **2017**, *8*, 68–103.

(5) Ugeda, M. M.; Bradley, A. J.; Shi, S.-F.; da Jornada, F. H.; Zhang, Y.; Qiu, D. Y.; Ruan, W.; Mo, S.-K.; Hussain, Z.; Shen, Z.-X.; Wang, F.; Louie, S. G.; Crommie, M. F. *Nature Materials* **2014**, *13*, 1091–1095.

(6) Liang, Q.; Zhang, Q.; Zhao, X.; Liu, M.; Wee, A. T. S. *ACS Nano* **2021**, *15*, 2165–2181.

(7) Tonndorf, P.; Schmidt, R.; Schneider, R.; Kern, J.; Buscema, M.; Steele, G. A.; Castellanos-Gomez, A.; van der Zant, H. S. J.; de Vasconcellos, S. M.; Bratschitsch, R. *Optica* **2015**, *2*, 347–352.

(8) Mitterreiter, E. et al. *Nature Communications* **2021**, *12*, 3822.

(9) Zinkiewicz, M.; Woźniak, T.; Kazimierczuk, T.; Kapuscinski, P.; Oreszczuk, K.; Grzeszczyk, M.; Bartoš, M.; Nogajewski, K.; Watanabe, K.; Taniguchi, T.; Faugeras, C.; Kossacki, P.; Potemski, M.; Babiński, A.; Molas, M. R. *Nano Letters* **2021**, *21*, 2519–2525.

(10) Nagler, P.; Ballottin, M. V.; Mitioglu, A. A.; Durnev, M. V.; Taniguchi, T.; Watanabe, K.; Chernikov, A.; Schüller, C.; Glazov, M. M.; Christianen, P. C. M.; Korn, T. *Physical Review Letters* **2018**, *121*, 057402.

Some journals require a graphical entry for the Table of Contents. This should be laid out "print ready" so that the sizing of the text is correct.

The space available depends on the journal: J. Am. Chem. Soc. allows 3.25 in by 1.75 in and requires sanserif text. Some journals want different sizes: you can easily adjust here.

The two rules either side of the content are there to help judge the height of your material: they may be deleted once not required.